6.1. Introduction

The $Nd_{0.7}Ba_{0.3}Mn_{1-x}Ti_xO_3$ manganites investigated in earlier chapters have the paramagnetic to ferromagnetic transition temperature below room temperature. Substitution of Ti-ions at the Mn-sites decreases the paramagnetic to ferromagnetic transition at further lower temperatures. For the potential applications in the field of science and advance technology, Curie temperature T_C should be close to the room temperature. We therefore, selected to investigate the effect of Ti-substitution at the Mn-site on the structure and magnetic properties of another system $La_{1-x}Ba_xMnO_3$ which has T_C above room temperature for a wide composition range. As discussed in Chapter 1, Ju et al. (2000) have reported the structural phase diagram of $La_{1-x}Ba_xMnO_3$ perovskite manganites for $0 \leq x \leq 0.5$ at room temperature. It shows tetragonal structure for $x < {\sim}0.13$, rhombohedral structure for ${\sim}0.13 < x < {\sim}0.38$ and cubic structure for ${\sim}0.38 < x < {\sim}0.50$. But for $x > 0.5$, they found coexistence of two crystallographic phases; cubic and unidentified phase. The Phase fraction of cubic phase decreases and unidentified phase increases with increase of doping concentration of Ba for $x > 0.5$. The $La_{1-x}Ba_xMnO_3$ perovskite manganites exhibit ferromagnetic (FM) behavior for $0.2 < x < 0.5$, in which samples having $x > 0.25$ show FM above room temperature. Jiang et al. (2008) studied $La_{1-x}Ba_xMnO_3$ $(0.1 \leq x \leq 0.3)$ series of single crystals and they observed that all samples exhibit Griffiths like singularity above room temperature.

In this chapter, we present the results of microstructural, elemental, structural and magnetic studies on $La_{1-x}Ba_xMnO_3$ with $x = 0.4$ using high resolution scanning electron microscopy (HR-SEM), energy dispersive X-ray spectroscopy (EDS), X-ray diffraction (XRD), and temperature and field dependent magnetization measurements, respectively.

6.2. Experimental Details

The nanocrystalline and bulk samples of $La_{0.6}Ba_{0.4}MnO_3$ perovskite manganites were synthesized by glycine-nitrate combustion synthesis method [Kumar et al. (2017)] as detailed in Chapter 2. The $La_{0.6}Ba_{0.4}MnO_3$ manganite is denoted by LBMO-40 throughout this chapter. The as prepared powder of LBMO-40 manganite after combustion synthesis was calcined at two different temperatures i.e. 900 and 1300°C for 6 hrs to get the nanocrystalline and bulk samples, respectively. The phase purity and crystal structure of the samples were examined by X-ray diffraction (XRD) patterns. The structural analysis of the samples was carried out using FullProf Suite [Carvajal (1993)]. Microstructures of the samples were analyzed by HR-SEM and elemental analysis was performed by EDS spectrum analysis. The HR-SEM micrographs were recorded on pellet samples prepared by using 2% aqueous solution of PVA (polyvinyl alcohol). The magnetic measurements (temperature and field dependence of magnetizations, frequency dependence of ac susceptibility) were performed by Quantum design superconducting quantum interference device (SQUID) magnetometer.

6.3. Results and Discussion

### 6.3.1. Structural Analysis: Rietveld Refinement

Fig. 6.1(a) demonstrates the powder XRD patterns of the $La_{0.6}Ba_{0.4}MnO_3$ samples calcined at 900 (nano) and 1300°C (bulk) recorded at room temperature. No, any secondary impurity phase was detected in the XRD pattern of the sample calcined at 1300°C, while, a small impurity peak of $BaMnO_3$ denoted by asterisk (*) (JCPDS File No.: 71-1595) was observed at $2\theta = 25.9°$ in the XRD pattern of the sample calcined at 900°C. The fraction of the impurity phase is less than 2% as determined from Rietveld analysis. The XRD patterns of both the bulk and nano samples of $La_{0.6}Ba_{0.4}MnO_3$ can be indexed using cubic structure with $Pm\overline{3}m$ space group as there is no peak splitting

for any lower symmetry phase. Contribution of particle size and strain broadening in the FWHM of diffraction peaks width for the nano sample were estimated using Williamson-Hall (W-H) method given by Equation (6.1):

$$\beta_{hkl} \cos\theta_{hkl} = 0.89 \ \lambda/d + 4\varepsilon \ \sin\theta_{hkl} \qquad (6.1)$$

where, β_{hkl} is FWHM corresponding to the diffraction peaks (hkl), λ is the radiation used during experiment (λ = 1.5406 Å), d is the average crystallite size, θ_{hkl} is Bragg's angle of corresponding reflection plane (hkl) and ε is the average value of lattice strain introduced within the lattice planes [Kumar et al. (2018a)]. **Fig. 6.1**(b) shows representative W-H plot between $\beta\cos\theta$ and $4\sin\theta$ for the nano sample of LBMO-40 manganite. The experimental data were fitted by straight line. The average values of crystallite size and lattice strain of the nano sample were found to be 32.3 nm and 1.7×10^{-3}, respectively as determined from the intercept and slope of the straight line.

The Rietveld structure refinement of the nanocrystalline and bulk samples was performed by using cubic $Pm\overline{3}m$ space group considering substitution of La-sites by Ba^{2+} cations. In the cubic crystal structure having $Pm\overline{3}m$ space group, Mn^{3+}/Mn^{4+} ions occupy 1(a) site at (0, 0, 0), La^{3+}/Ba^{2+} ions occupy at 1(b) site at (1/2, 1/2, 1/2) and O^{2-} anions occupy 3(c) site at (1/2, 0, 0). **Figs. 6.1**(c) and (d) display Rietveld fits for the XRD patterns of nano and bulk samples of LBMO-40 manganite, respectively. Solid dots indicate experimentally obtained XRD profile, while the continuous line overlapping to the solid dots shows simulated XRD pattern. The vertical bars in the figure display position of Bragg's reflections and the lower curve indicates difference profile between experimental and simulated XRD patterns. The Rietveld fits are quite good confirming the cubic crystal structure of bulk and nano LBMO-40 manganite.
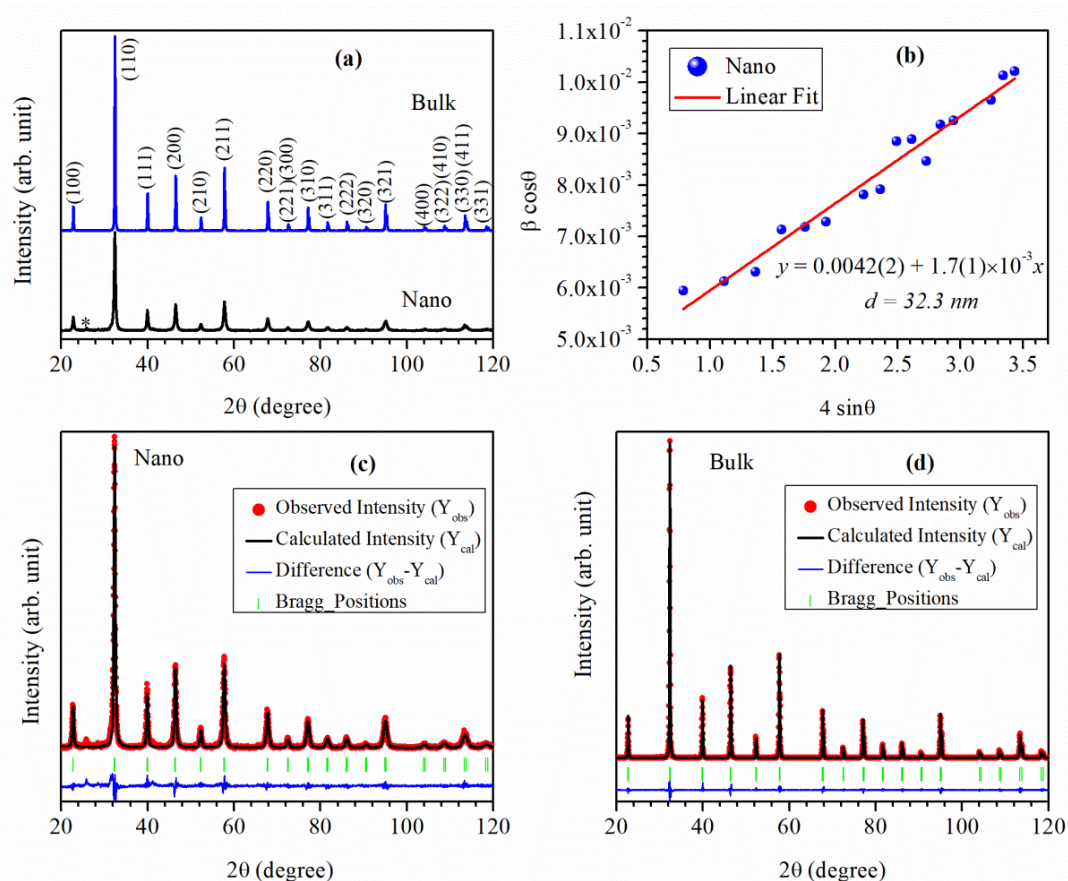
Figure 6.1: (a) RT powder XRD patterns for LBMO-40 manganites calcined at 900 and 1300°C temperatures. (b) A representative W-H plot for the nano sample of LBMO-40 manganite. Rietveld fits for (c) nano and (d) bulk samples of LBMO-40 manganite.

The lattice parameter "a" and unit cell volume "V" decrease with increasing calcination temperature from 3.9120(2) Å for nano to 3.9097(1) Å for bulk and 59.869(4) Å^3 for nano and 59.764(1) Å^3 for bulk, respectively. The bond-lengths Mn-O and La-O were calculated from the Rietveld structure refinement. The Mn-O bond-length decreases from 1.95600(8) Å to 1.95486(3) Å and La-O bond length from 2.76621(8) Å to 2.76459(3) Å with increasing particle sizes from nano to bulk. **Figs. 6.2**(a-b) display MnO$_6$ octahedra along with Mn-O bond-length for nano and bulk samples, respectively. **Fig. 6.2**(c) represents schematic ball and stick unit cell for LBMO-40 manganite. The Mn-site is surrounded by six oxygen atoms forming MnO$_6$

166

octahedra and La/Ba-site atoms is surrounded by twelve oxygen atoms to forms La/BaO$_{12}$.
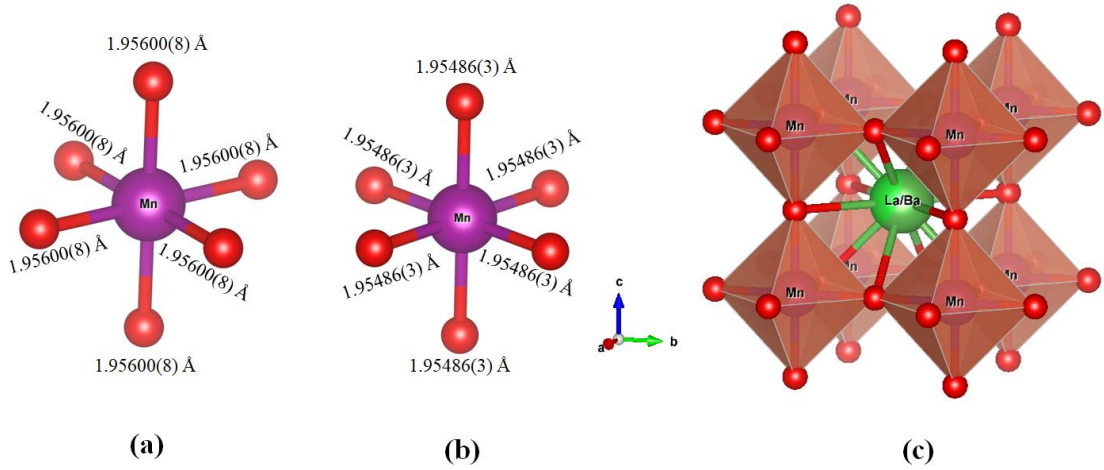

Figure 6.2: (a-b) MnO$_6$ octahedra for nano and bulk LBMTO-40 manganite showing Mn-O bond lengths for each, respectively. (c) Schematic Ball and Stick unit cell for LBMO-40 manganite.

6.3.2. Microstructural and Elemental Analysis

The characteristic high resolution scanning electron microscopy (HR-SEM) images of the LBMO-40 samples calcined at 900 and 1300°C are shown in **Figs. 6.3**(a) and (b), respectively. The mean value of particle size was determined using ImageJ software by including as many particles as possible in our calculation. The average particle size is found to be 35 and 500 nm for the samples calcined at 900 and 1300°C, respectively. The crystallite size estimated from W-H plot and particle size calculated using HR-SEM micrograph for nano sample are approximately equal. **Figs. 6.3**(c-d) show energy dispersive X-ray spectroscopic (EDS) spectra for the nano and bulk samples of LBMO-40 manganite, respectively. The appearance of characteristic peaks for La, Ba, Mn and O in the EDS spectra shows the presence of constituent elements in the samples. Since experimental technique of EDS is not suitable for the lighter

elements like oxygen. So, we have performed the qualitative analysis of the nominal compositions excluding oxygen element for both the samples. The results of quantitative analyses for the composition are presented in **Table 6.1**. The experimental and theoretical values of atomic percentages are very close to each-other within the limit of experimental error.
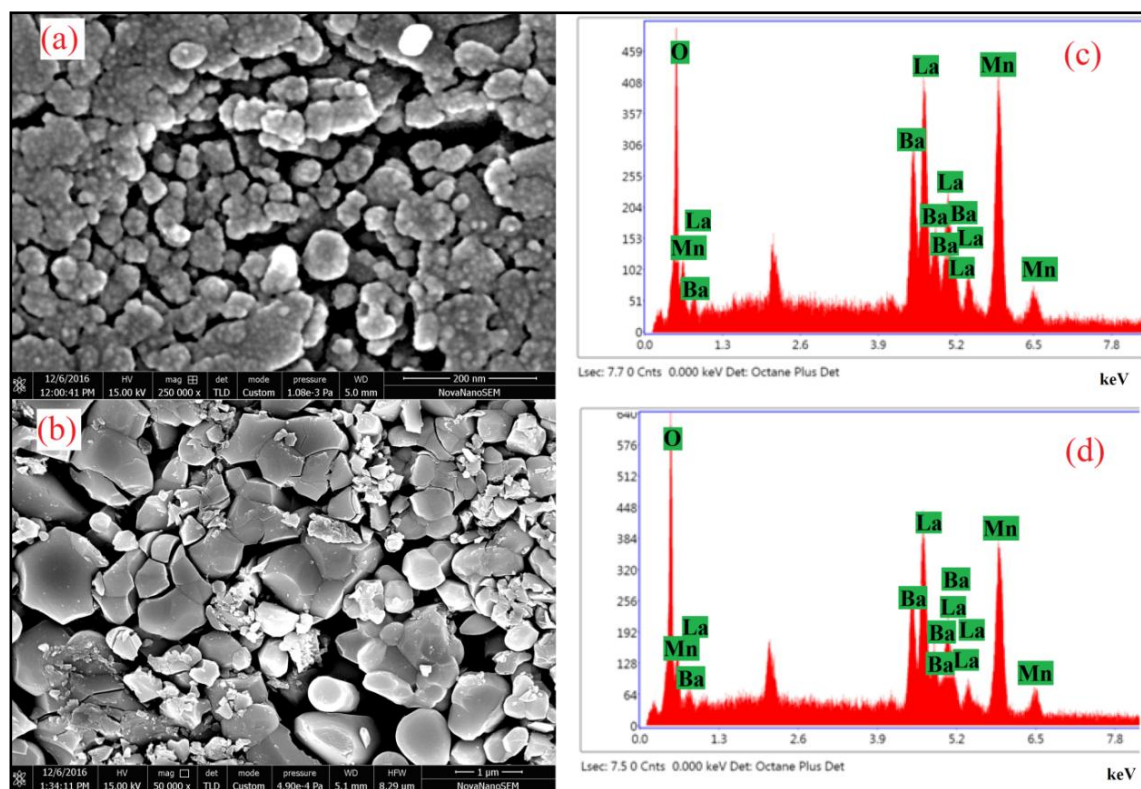
Figure 6.3: (a-b) High resolution scanning electron microscopy (HR-SEM) images and (c-d) Energy dispersive X-ray spectroscopy (EDS) spectra for nano and bulk samples of $La_{0.6}Ba_{0.4}MnO_3$ manganites, respectively.

Table 6.1: Experimental and theoretical atomic percentages obtained from EDS spectrum for nano and bulk samples of LBMO-40 manganite.

| Element	Nano		Bulk	
	Atomic%		Atomic%	
	Exp.	Theo.	Exp.	Theo.
Ba	19.06	20	17.46	20
La	29.01	30	30.15	30
Mn	51.93	50	52.39	50
Totals	100.00			

6.3.3. Magnetic Properties

6.3.3.1. Temperature Dependent Magnetization Studies

The temperature dependence of magnetization M(T) was measured in a constant applied magnetic field of 200 Oe under zero field cooled (ZFC) and field cooled (FC) conditions in the temperature range of 2-390 K. During the ZFC magnetization measurements, samples were first cooled from 390 to 2 K in the absence of magnetic field, while in the case of FC, samples were cooled in the presence of an applied field. Then the magnetization was recorded in warming mode from 2 to 390 K. **Fig. 6.4**(a) shows M(T) plots for the nano and bulk samples of LBMO-40 manganite recorded in ZFC and FC modes at H = 200 Oe. The ZFC magnetization curves for both the samples exhibit a large broad maxima peak (T_B) and both the samples (Nano and Bulk) undergo PM to FM phase transition above room temperature. The values of T_C have been determined by the minima appearing in the dM/dT vs. T plots as shown in **Fig. 6.4**(b) for both the samples. Appearance of FM ordering is explained in terms of double exchange (DE) interaction between Mn^{3+} and Mn^{4+} cations through O^{2-} anion, i.e., Mn^{3+}-O^{2-}-Mn^{4+} network [Zener (1951)] as discussed in chapter 1. As the particle size increases from nano (35 nm) to bulk (500 nm), T_C shifted towards the higher

temperature side. The T_C is found to be 315 and 330 K for nano and bulk LBMO-40, respectively. Reduction in T_C suggests the weakening of DE interaction with decrease in particle size of the LBMO-40 manganite. A similar result in the 30 mol% Ca-doped LaMnO$_3$ (i.e., La$_{0.7}$Ca$_{0.3}$MnO$_3$) manganite system was also observed, where T_C decreases with decreasing particle size [Phong et al. (2016b)]. As the temperature is lowered, the ZFC and FC magnetizations curves for nano and bulk samples start deviating from each other below 338 K. The irreversibility between in the ZFC and FC magnetizations (i.e., $M_{irr} = M_{FC} - M_{ZFC}$) increases with lowering temperature and particle size, this may be due to inhomogeneous magnetic ordering that may due to competition between FM and AFM ordering. A very large irreversibility between FC and ZFC magnetizations for nano sample of LBMO-40 is observed, this shows large competition between AFM and FM ordering in low temperatures regime than the bulk sample. A representative M_{irr} vs. T plots for both the samples are shown in **Fig. 6.4**(c). A clear peak in the vicinity of FM transition T_C in irreversible magnetization curve is observed as shown in the zoomed view of inset of **Fig. 6.4**(c). A similar result was also observed in Nd$_{0.84}$K$_{0.12}$MnO$_3$ manganite by Samantaray et al. (2010).

As discussed in the previous section, analysis of the powder XRD pattern of nano sample reveals an impurity phase of BaMnO$_3$ (less 2%). The BaMnO$_3$ exhibits AFM ordering below 220 K [Korneta et al. (2011)]. But, in the magnetization measurements, we do not observe any transition near 220 K in both the bulk and nano samples (see **Fig. 6.4**(b)). This suggests that there is no contribution of BaMnO$_3$ to the magnetic response of the samples. Hence during calculation of effective paramagnetic and saturation moments (next sections), we do not consider the effect of BaMnO$_3$ impurity present in the nano sample of LBMO-40 manganite.
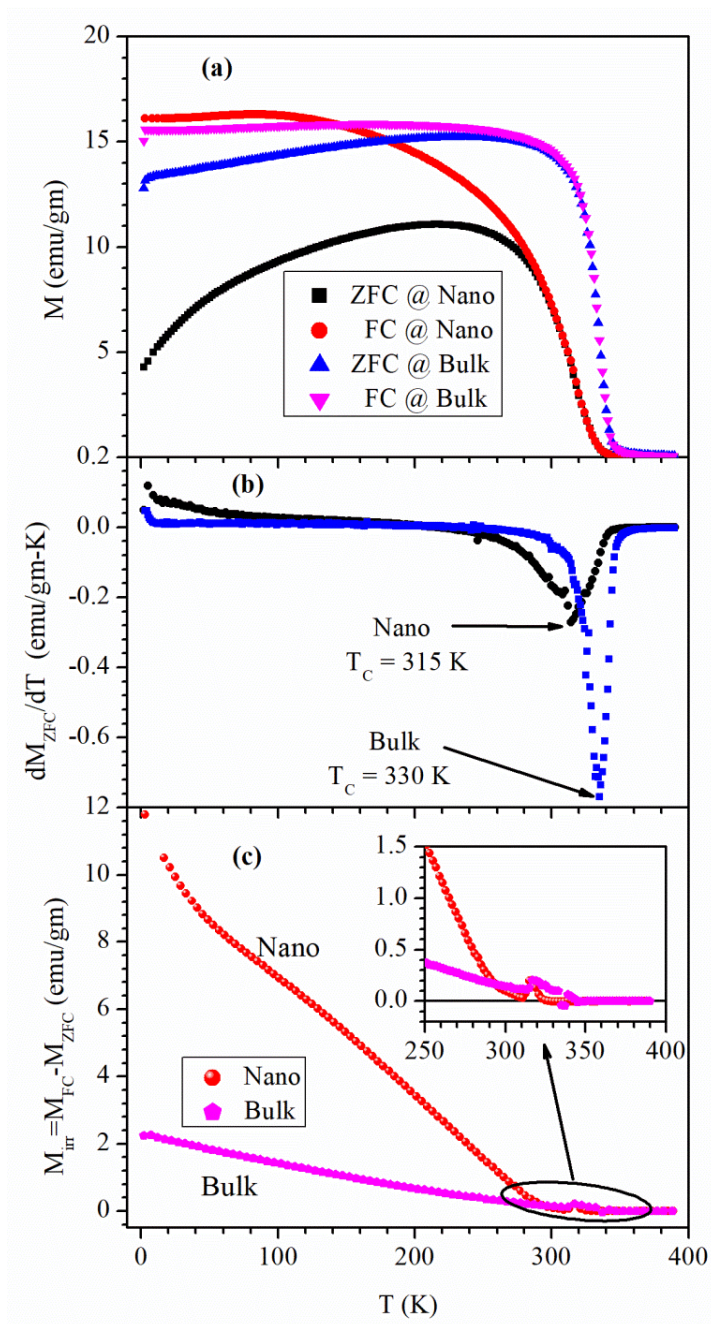
Figure 6.4: (a) Temperature dependence ZFC and FC magnetization curves, (b) dM_{ZFC}/dT vs. T plots and (c) variation of irreversible magnetization as a function of temperature for nano and bulk samples of LBMO-40 manganite. Inset of (c) indicates zoomed view of the irreversible magnetization near T_C.

6.3.3.2. Temperature Dependent Inverse dc Susceptibility Studies

The temperature dependence of inverse dc and real part ac molar susceptibility [$\chi^{-1}(T)$] for nano and bulk samples of LBMO-40 manganite are presented in **Figs. 6.5**(a) and (c) in the temperature range of 300-390 K, respectively. The high temperature PM region $\chi^{-1}(T)$ follows Curie-Weiss (CW) law described by Equation (6.2):

$$\chi^{-1}(T) = (T - \theta_{CW})/C \tag{6.2}$$

where, θ_{CW} is CW temperature and C is Curie constant. The values of θ_{CW} and C can be estimated by fitting straight line in the PM region. The value of θ_{CW} was calculated by the intercept value of straight line to the temperature axis and C was estimated by taking inverse of the slope of straight line. From the dc inverse molar susceptibility, the linear (CW law) fit in the PM regime for nano and bulk samples reveal that nano sample exhibits $\theta_{CW} \sim 324.28$ K and C ~ 2.58 emu-K/Oe-mol, while, bulk sample shows $\theta_{CW} \sim$ 339.45 K and C ~ 4.05 emu-K/Oe-mol. The values of θ_{CW} and C were also determined from the ac inverse molar susceptibility measured at lowest frequency of 100 Hz. The values of θ_{CW} and C for the nano sample are found to be ~323.4 K and ~2.59 emu-K/Oe-mol, respectively and 338.40 K and 4.05 emu-K/Oe-mol for bulk sample, respectively. The obtained values of θ_{CW} and C from dc as well as ac susceptibility for higher frequencies (300 & 500 Hz) are found to be approximately identical for both nano and bulk samples of LBMO-40 manganite. We can compare theoretical and experimental values of effective paramagnetic moment for both the samples. Theoretical effective paramagnetic moment in the unit of Bohr magneton (μ_B) per molecular formula can be found out using the relation (6.3) given below:

$$\mu_{eff}^{theo} (\mu_B) = \sqrt{0.6 \times \mu_{Mn^{3+}}^2 + 0.4 \times \mu_{Mn^{4+}}^2} \tag{6.3}$$

Where, $\mu_{Mn}^{3+} = 4.9$ μ_B and $\mu_{Mn}^{4+} = 3.87$ μ_B are effective paramagnetic moment of Mn^{3+} and Mn^{4+} ions, respectively [Phong et al. (2016b)]. The calculated theoretical value of

effective PM moment is found to be 4.52 μ_B. However, the experimental value of effective PM moment was calculated in the unit of Bohr magnetron with the help of following formula given in Equation (6.4):

$$\mu_{eff}^{exp} (\mu_B) = \sqrt{3k_B C / N_a \mu_B^2} = \sqrt{8C} \qquad (6.4)$$

Where, k_B and N_a are Boltzmann constant and Avogadro number, respectively [Phong et al. (2016b)]. The estimated experimental values of effective PM moment for nano and bulk samples of LBMO-40 were found to be 4.55 and 5.69 μ_B, respectively that are greater than their theoretical values. This can be attributed to the presence of FM component within the PM region [Phong et al. (2016b)].
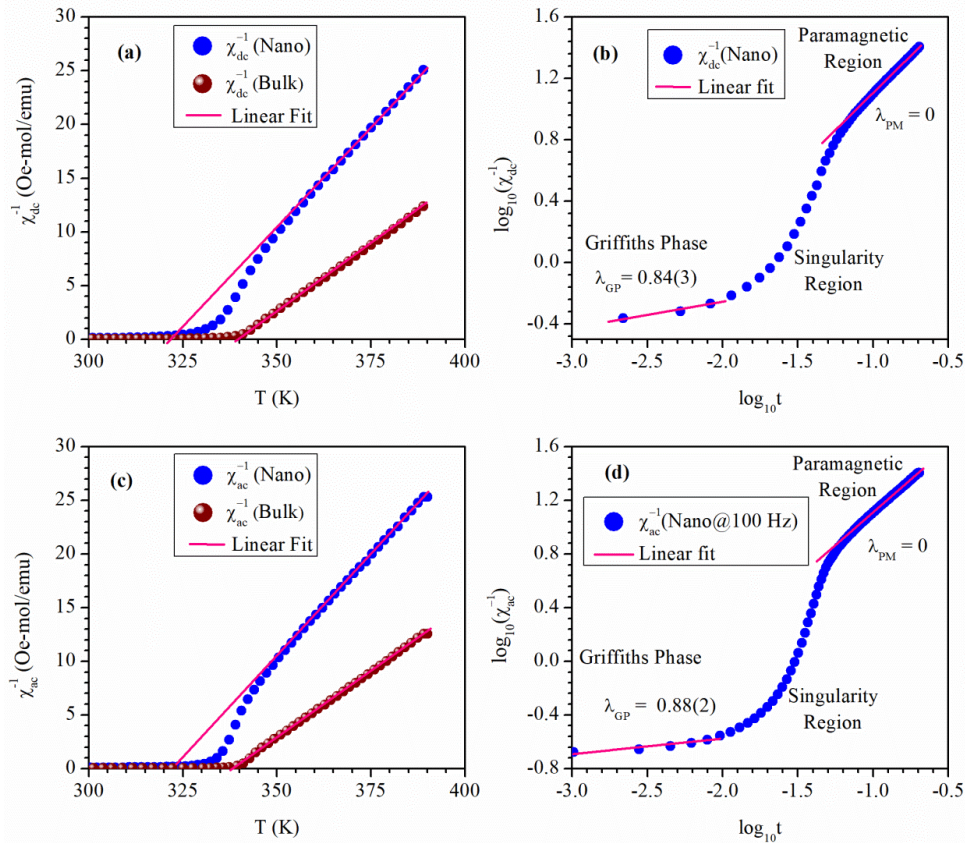
Figure 6.5: (a) & (c) Variation of inverse dc molar susceptibility as a function of temperature for nano and bulk samples of LBMO-40, in which dots display experimental data while straight lines show CW fits at higher temperatures. (b) & (d) $log_{10}t$ versus $log_{10}\chi^{-1}$ plot for the nano sample of LBMO-40 manganite.

6.3.3.3. Griffiths Phase Analysis

As can be seen from **Fig. 6.5**, the $\chi^{-1}(T)$ for nano sample deviates significantly from CW law in the lower temperature region well above T_C. Appearance of sharp downward deviation in $\chi^{-1}(T)$ for nano sample provides signature of Griffiths phase (GP) singularity above Curie temperature [Shankar et al. (2018); Pramanik et al. (2010)]. However, for the bulk sample, there is no clearly visible Griffith's phase-like feature. The onset temperature where $\chi^{-1}(T)$ starts deviating from CW law is identified as Griffiths' temperature T_G. Signature of GP may be due to magnetic inhomogeneity present in PM regime [Shankar et al. (2018)]. Existence of GP is supposed to lie between the temperature range $T_C \leq T \leq T_G$, where no spontaneous magnetization can be observed due to the deficiency of any long-range static FM order [Phong et al. (2016b)]. Usually, in the region of GP singularity, inverse susceptibility must follow modified CW law (or power law) given by Equation (6.5):

$$\chi^{-1}(T) \propto \left|T - T_C^R\right|^{1-\lambda} \tag{6.5}$$

where, T_C^R is critical temperature for random ferromagnet and λ is critical exponent for GP and lies between $0 \leq \lambda \leq 1$ [Pramanik et al. (2010); Shankar et al. (2018); Phong et al. (2016b); Jiang et al. (2008); Karmakar et al. (2012)]. The extent of λ is the identification of the extent of the GP, higher value of λ means greater extent of GP. As discussed in chapter 5 also, the assessment of value of T_C^R is crucial for precise determination of λ. The value of T_C^R is choosen such that in PM region one can get $\lambda = 0$. It is convenient to choose $T_C^R = \theta_{CW}$ [Karmakar et al. (2012)]. To estimate the critical exponent λ, we plotted a curve between $\log_{10}t$ and $\log_{10}\chi^{-1}$ (**Fig. 6.5**(b)), where $t = (T/T_C^R-1)$ is reduced temperature. **Figs. 6.5**(b) and (d) shows log-log plots between reduced temperature and inverse susceptibility of dc and ac susceptibilities for the nano sample, respectively. In this figure, two linear regions are identified one corresponds to

PM ordering for which λ is equal to zero and second corresponds to GP region for which λ is non-zero and less than unity. In between these regions singularity region exists. The value of critical exponent λ from dc and real part of ac susceptibility was found to be λ_{GP} = 0.84(3) and 0.88(2), respectively. Reasonably large values obtained for λ_{GP} point out the sturdiness of the GP in this manganite system. Karmakar et al. (2012) also found such a large value of λ_{GP} for the antiferromagnetically ordered $La_{0.32}Eu_{0.68}MnO_3$ manganite. The other manganite systems like $La_{0.7}Ba_{0.3}MnO_3$ [Jiang et al. (2008)], $Sm_{0.5}Sr_{0.5}MnO_3$ [Zhou et al. (2011)], Ga-doped $Pr_{0.5}Sr_{0.5}MnO_3$ manganite [Pramanik et al. (2010)], $La_{0.7}Ca_{0.3}MnO_3$ [Phong et al. (2016b)] etc. also show large value of critical exponent λ in GP regime.

6.3.3.4. Field Dependent Magnetization Studies

To further explore the magnetic behavior (quantitative analysis) of the samples, field dependent magnetization M(H) measurements were performed at 10 and 300 K (RT) in the magnetic field range from -60 kOe to +60 kOe. **Figs. 6.6**(a-b) demonstrate field dependent magnetization curves for nano and bulk samples of LBMO-40 manganite. In the low-field region, field dependent magnetization increases very sharply below magnetic field of 1 kOe and above this field M(H) increases slowly for the both samples at both measurement temperatures. At 10 K, magnetization of the nano sample of LBMO-40 manganite above 5 kOe increases gradually and remains unsaturated even up to magnetic field of 60 kOe. The non-saturation behavior of the M(H) curve shows the existence of short-range AFM ordering in nano sample. In contrast, the M(H) curve of bulk sample gets saturated above 15 kOe due to complete alignment of the spins of the Mn^{3+} and Mn^{4+} ions. At 300 K, both the bulk and nano samples show unsaturation behavior of M(H) curves which is due to PM contribution in FM ordering for the LBMO-40 manganite. The reduction in the saturation of magnetic hysteresis loops with

increasing temperature is due to ferromagnetic spin disorder present in the system [Mohamed et al. (2017)]. **Figs. 6.6**(c-d) show magnetic hysteresis loops for nano and bulk samples of LBMO-40 manganite, respectively. The inset of **Figs. 6.6**(c-d) show low-field zoomed picture of the magnetic hysteresis loops, which further confirm the FM nature of the system. The values of the remanence magnetization (M_r) and coercive field (H_C) were estimated and were found to be M_r = 16.0 & 1.3 emu/gm and H_C = 265 & 22 Oe for nano sample at 10 and 300 K, respectively. For bulk sample, M_r = 2.6 & 0.9 emu/gm and H_C = 28 & 10 Oe at 10 and 300 K, respectively. The very small values of M_r and H_C for bulk LBMO-40 manganite indicate that LBMO-40 manganite is a soft ferromagnet. To find out the fraction of FM ordering present in the samples, we have estimated theoretical and experimental values of saturation moment. The spin only theoretical value of saturation moment $\mu_{sat}^{theo}\left(\mu_B/f.u.\right)$ per formula unit in the units of Bohr magneton was calculated using the expression given by Equation (6.6), considering full alignment of spins of Mn^{3+} and Mn^{4+} ions in parallel direction [Phong et al. (2016b)]:

$$\mu_{sat}^{theo}\left(\mu_B/f.u.\right) = 0.6M_{Mn^{3+}} + 0.4M_{Mn^{4+}} \tag{6.6a}$$

$$\mu_{sat}^{theo}\left(\mu_B/f.u.\right) = 2\mu_B\left[0.6\times\frac{4}{2} + 0.4\times\frac{3}{2}\right] \tag{6.6b}$$

The theoretical value of saturation moment is found to be 3.60 μ_B. However, experimental value of saturation moment $\mu_{sat}^{exp}\left(\mu_B/f.u.\right)$ (in the unit of Bohr magneton) is calculated with the help of following Equation (6.7):

$$\mu_{sat}^{exp}\left(\mu_B/f.u.\right) = M_{sat}^{exp}\, M_m/N_a\mu_B \tag{6.7}$$

Here, N_a is Avogadro's number, M_m (= 241.2013 gm/mol) is molar mass of the sample, M_{sat}^{exp} is the experimental value of saturation magnetization and μ_B is Bohr magneton [Phong et al. (2016b)]. The experimental value of saturation magnetization was estimated by extrapolating straight line from higher magnetic field to zero magnetic

field, as shown in **Figs. 6.6**(a-b) for nano and bulk samples of LBMO-40 manganite. The calculated values of saturation moment were found to be 0.97 μ_B (%FM = 27%) and 2.36 μ_B (%FM = 66%) measured at 300 and 10 K, respectively, for nano sample of LBMO-40. For bulk sample, saturation moment were found to be 2.37 (%FM = 66%) and 3.93 μ_B (%FM = 100%) for M(H) curves measured at 300 and 10 K, respectively. Experimental value of saturation moment obtained for M(H) at 10 K for the bulk sample of LBMO-40 manganite is greater than the spin only theoretical value of saturation moment. This may be due to orbital contribution in the saturation moment. However, for the nano sample, the experimental saturation moment is less than the theoretical value of saturation moment, which shows the absence of spin-orbital coupling. This suggests that quenching of spin-orbital coupling can be achieved by reducing particle size of the LBMO-40 manganite. The orbital contribution in saturation moment at low temperature (10 K) in bulk sample was estimated after assuming complete parallel alignments of the spins of Mn^{3+} and Mn^{4+} cations and found to be ~ 9 % of the spin-only moment.
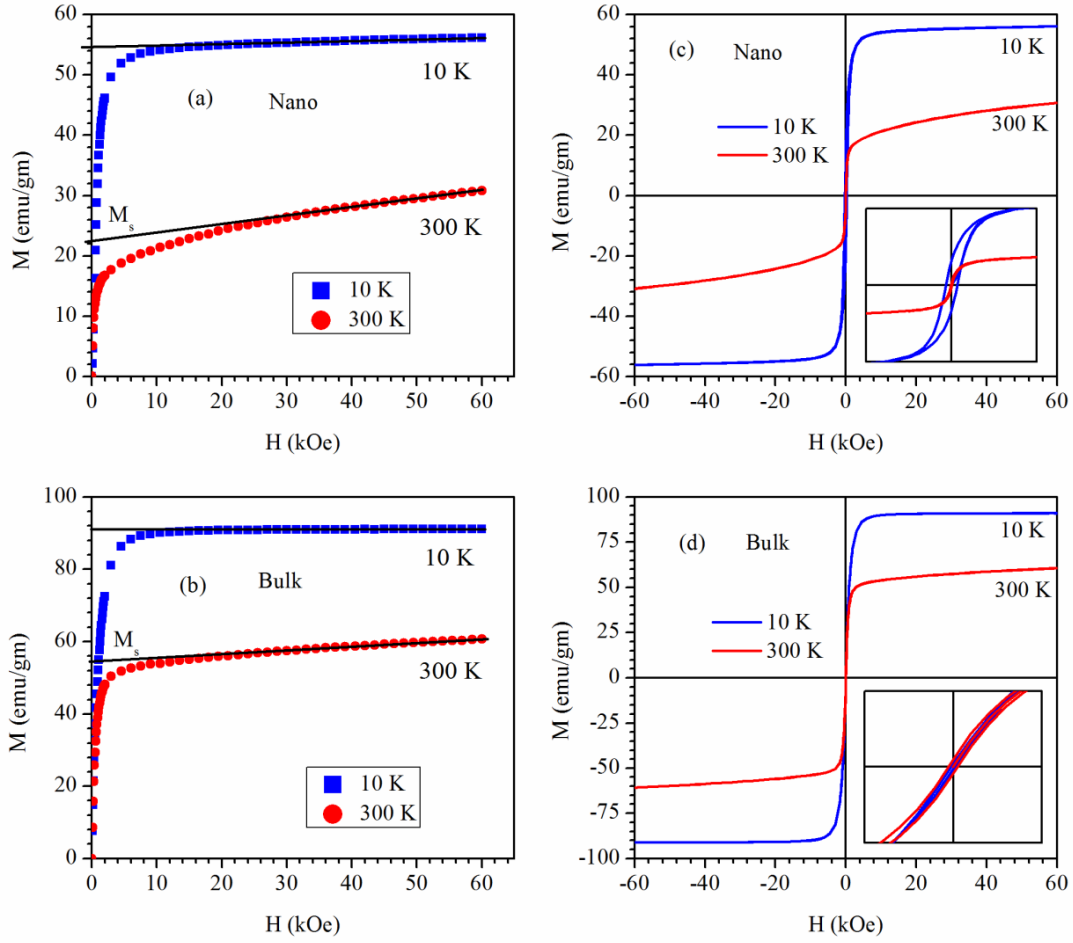
Figure 6.6: (a-b) Field dependence of magnetization M(H) curves and (c-d) isothermal magnetic hysteresis loops for nano and bulk samples of LBMO-40 manganite measured at 10 and 300 K temperatures. Insets of (c-d) show the low filed zoomed view of the hysteresis loops.

As discussed in Chapter 3, according to the mean field theory, the Gibbs free energy (G) of the magnetic system can be expressed as a function of magnetization and temperature as given by Equation (6.8):

$$G\,(T,\,M) = G_0 + \tfrac{1}{2}\,AM^2 + \tfrac{1}{4}\,BM^4 - MH \tag{6.8}$$

where, G_0 is temperature independent constant, and A and B are temperature dependent constants [Phong et al. (2017)]. For the equilibrium of the system near T_C the first

derivative of the free energy with respect to magnetization must be zero, i.e. $\delta G/\delta M = 0$, which gives equation of state given by (6.9):

$$H/M = A + BM^2 \tag{6.9}$$

Thus, the nature of the PM-FM phase transition can be seen more clearly from the isothermal Arrott's plots of M^2 vs. H/M [Phong et al. (2017); Kumar et al. (2019)]. **Figs. 6.7**(a-b) present isothermal Arrott's plots for nano and bulk samples of LBMO-40 manganite, respectively, and insets show zoomed view of Arrott's plots in the low value region of H/M. At high H/M values, the Arrott's plots are straight lines, which intersect M^2-axis (H = 0). These features indicate existence of long-range FM ordering. The intercept value of magnetization at H = 0 is known as spontaneous magnetization M_0 for ferromagnets. The value of M_0 decreases with increasing temperature and particle sizes of the samples. The values of M_0 were found to be 54.65 and 17.41 emu/gm for nano sample at 10 and 300 K temperature, respectively, while, for bulk sample, these are 91.15 and 53.20 emu/gm at 10 and 300 K, respectively. Furthermore, according to the Banerjee's criterion [Banerjee (1964)], if the symptom of the slope for every isothermal M^2 vs. H/M curves is positive, then the behavior of the magnetic transition will be of second-order. If the slope is negative, then the nature of magnetic transition will be of first-order. The isothermal Arrott's plot for the nano sample measured at 10 K shows negative slope, while, both isothermal Arrott's plots for bulk sample demonstrate positive slope. Thus, according to the Banerjee's criterion, nano sample of LBMO-40 exhibit first order magnetic transition (FOMT) while bulk sample exhibit second order magnetic transition (SOMT) in the low field region and both samples shows SOMT in the high field region. Doshi et al. reported that Tb^{3+}-doped $La_{0.5}Ca_{0.5}MnO_3$ manganite shows FOMT in the low field region, and switches to SOMT for the higher magnetic field above 10 T [Doshi et al. (2011)].
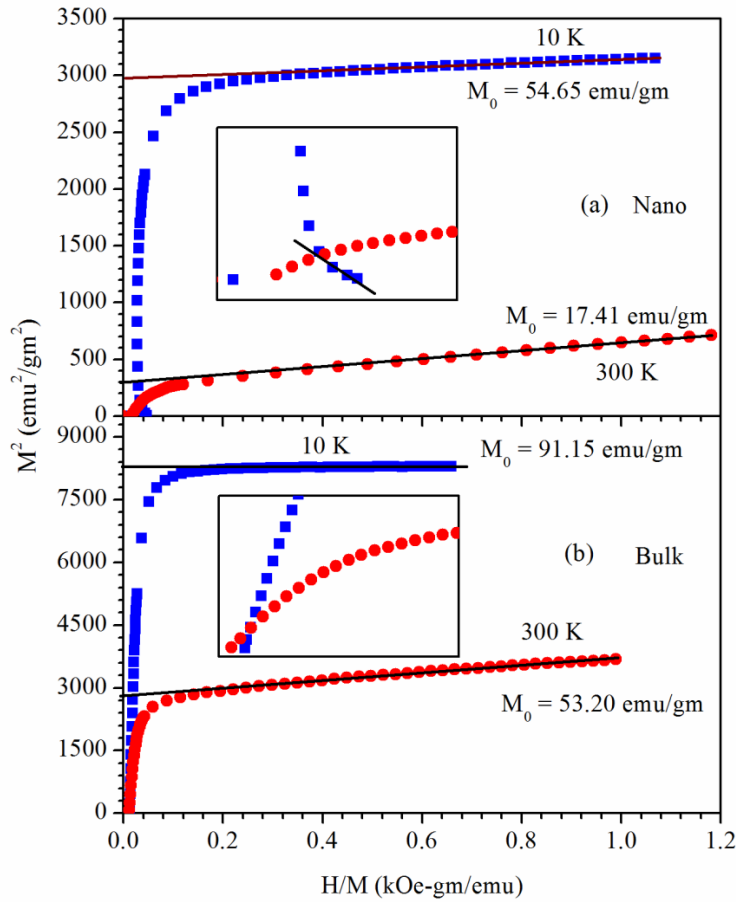
Figure 6.7: (a-b) Isothermal Arrott's plots M^2 vs. H/M for nano and bulk samples of LBMO-40 manganite, respectively.

6.3.3.5. Temperature Dependent ac Susceptibility Studies

Fig. 6.8 shows the temperature dependent real $\chi'(T)$ and imaginary part $\chi''(T)$ of ac susceptibility for nano and bulk samples of LBMO-40 manganite, measured in the presence of very small ac magnetic field and at different frequencies i.e., 100, 300 and 500 Hz. It is obvious from ac susceptibility plots that both samples clearly show PM to FM phase transition at T_C. The qualitative behavior of the real part of ac susceptibility curves is similar to the dc ZFC magnetization curves. The real part of the ac susceptibility shows broad maxima peak near T_B, which is frequency independent.
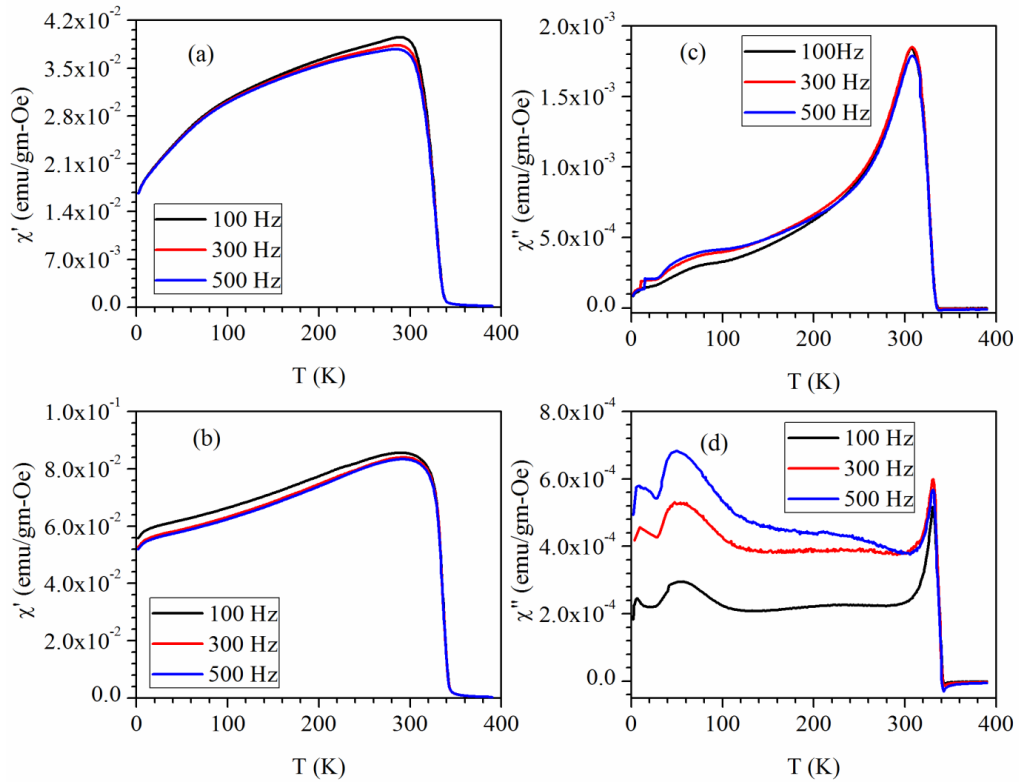
Figure 6.8: Temperature dependence of (a-b) real part and (c-d) imaginary part of ac susceptibility for nanocrystalline and bulk LBMO-40 samples, respectively measured at various frequencies.

However, the qualitative behavior of $\chi''(T)$ for nano and bulk samples is different from their respective $\chi'(T)$ and also from each other. The imaginary part of the ac susceptibility for both samples exhibits a frequency independent sharp main peak close to T_{irr} along with several anomalies in the low temperature region. The equivalent feature is not clearly visible in the real part of ac susceptibility and this may happen as a result of the large real part of the susceptibility associated with ferromagnetism [Roy et al. (2008)]. For nano sample, the $\chi''(T)$ in PM region is almost zero and increases sharply near T_C and exhibits maxima peak at T_{irr} and first decrease sharply and then smoothly with decreasing temperature below $T_{irr.}$ In the low temperature region it exhibits two anomalous peaks around ~78 K and ~12 K. For bulk sample, the $\chi''(T)$ increases quickly with decreasing temperature below PM region and shows maxima at

T_{irr}, below T_{irr} the value of $\chi''(T)$ decreases sharply and exhibits several anomalous peaks at different temperatures such as around 230, 55 and 8 K. The origin of these peaks in $\chi''(T)$ is being investigated and will be reported later on.

6.4. Conclusions

In summary, the nano and bulk samples of LBMO-40 manganite were synthesized via combustion synthesis process. The Rietveld refinement of the XRD patterns for nano and bulk samples of LBMO-40 reveals that LBMO-40 crystallizes into cubic crystal structure having $Pm\bar{3}m$ space group. The refined lattice parameter "a" and unit cell volume "V" decrease with increasing particle size from a = 3.9120(2) Å and V = 59.869(4) $Å^3$ for nano sample to a = 3.9097(1) Å and V = 59.764(1) $Å^3$ for bulk sample. Temperature dependent magnetization M(T) measurements for nano and bulk samples clearly demonstrates paramagnetic to ferromagnetic phase transition at Curie temperature T_C, which decreases with decreasing particles size from 330 K for bulk to 315 K for nano. A signature of Griffiths phase singularity is observed in nano sample. The percentage of FM fraction within the sample increases with increasing particle size (from nano to bulk) and decreasing measurement temperature (from RT to 10 K). Spontaneous magnetization M_0 of the ferromagnetic sample increases with lowering temperature (from RT to 10 K) and increasing crystallite size (from nano to bulk). A spin-orbital coupling was observed in the bulk sample of LBMO-40 manganite at low temperature (10 K), however, the nano sample does not exhibit spin-orbital coupling. Thus, the spin-orbital coupling is quenched by reducing particle size of the LBMO-40 manganite. According to the Banerjee's criterion, analysis of the Arrott's plots reveals that nano and bulk samples exhibit first and second order magnetic phase transition in the low magnetic field region, respectively. The behavior of the $\chi'(T)$ curves for nano and bulk samples are similar to their respective M_{ZFC} curves.